nature communications

Article

https://doi.org/10.1038/s41467-026-74088-8

Chiral emission from chirotopic nanostructures

Received: 12 May 2026

Accepted: 29 May 2026

Published online: 05 June 2026

Check for updates

Yawei Wu[1,2,10], Zhenyu Wang[1,10], Zihan Wu[1,10], Jiahui Xu[3], Chenlu He[4], Shuqing He[5], Ruize Wang[1], Mingsheng Gao[6], Qing Zhang[6], Chaowei Wang[1], Jincheng Ni[1], Zhipeng Li[7], Yiming Wu[8], Jiaru Chu[1], Dong Wu[1], Xiaogang Liu[3] ✉ & Yang Chen[1,9] ✉

Mirror asymmetry of electronic states or optical media is expected for the emission of chiral photons, which constrains the design of dichroic materials. Here we demonstrate that these symmetry restrictions can be relaxed by harnessing the local chirality of globally achiral materials, also known as chirotopicity. Unlike chirotopic sites in molecules whose optical effects are unknown, photonic nanostructures make possible the enhancement and deliberate localization of left- and right-handed chirotopic fields by linearly polarized light. We show that intense and highly elliptic light is emitted from achiral luminophores engulfed by such fields. Luminescence dissymmetry factors between 1.65 and −1.58, approaching the theoretical limit, are obtained for nanoparticles and dyes, which may be generalized to other luminophores. After being hypothesized by Mislow more than 50 years ago, these findings validate the concept of chirotopicity and enable its utilization in chiral photonics.

The symmetry of molecules, crystals and composites imposes fundamental limits on optical properties. For example, vector multiplication for electronic transitions in dipolar approximation restricts the emission of mirror-asymmetric circularly polarized photons to mirror-asymmetric electronic states[1–5]. This notion successfully guided the synthesis of a large body of luminescent molecules[6], polymers[7], crystals[8], and filaments[9] designed to be intense emitters of chiral photons. Circularly polarized light (CPL) can also be emitted by achiral luminophores when they are embedded into composites possessing helical structural motifs[10–18], extrinsic chirality[19,20], or specific combination of linear birefringence and linear dichroism[21,22]. Although the individual components and electronic states of the luminophores are mirror-symmetric, their global structures are not, which substantiates the necessity of global mirror asymmetry for CPL emission.

Such symmetry-based heuristic rules may, however, be too simplistic because these and other examples indicate that chirality is a scale-dependent parameter[23]. A material can be globally achiral, but the local environment of the electronic state can still be chiral. The difference between local and global asymmetry can be particularly important for the engineering of CPL emitters with high brightness and ellipticity, which have both fundamental and technological relevance. Dissymmetry g-factors $g_{lum} = 2\cdot(I_{RCP} - I_{LCP})/(I_{RCP} + I_{LCP})$ are often employed as a cumulative figure of merit for chiral luminophores and composites. There has been intense research and significant progress

[1]Department of Precision Machinery and Precision Instrumentation, University of Science and Technology of China, Hefei, China. [2]Hefei National Laboratory for Physical Sciences at the Microscale, University of Science and Technology of China, Hefei, Anhui, China. [3]Department of Chemistry, National University of Singapore, Singapore, Singapore. [4]School of Chemistry and Chemical Engineering, Nanjing University of Science and Technology, Nanjing, China. [5]College of Health Science and Environmental Engineering, Shenzhen Technology University, Shenzhen, China. [6]School of Physics, University of Electronic Science and Technology of China, Chengdu, China. [7]Anhui Province Key Laboratory of Integrated Circuit Science and Technology, University of Science and Technology of China, Hefei, People's Republic of China. [8]Institute of Flexible Electronics (IFE, Future Technologies), Xiang'an Campus, Xiamen University, Xiang'an South Road, Xiamen, Fujian, China. [9]State Key Laboratory of Opto-Electronic Information Acquisition and Protection Technology, Hefei, China. [10]These authors contributed equally: Yawei Wu, Zhenyu Wang, Zihan Wu. ✉e-mail: chmlx@nus.edu.sg; cyang_phys@ustc.edu.cn

of CPL emitters[24] with $g_{lum} > 0.5$. Nevertheless, g_{lum} remains 10^{-3}–10^{-2} for the majority of chiral molecules because the pursuit of high ellipticity in luminophores activates non-radiative decay, thereby limiting quantum yields[25].

In this work, we show that CPL emission can be attained by harnessing the local chirality of globally achiral nanostructures, which enables virtually any nanostructure or molecule to emit CPL. The concept of local chirality or chirotopicity was first introduced by Mislow in 1967 and refers to a geometric point in a molecule that cannot remain invariant under local rotation-reflection operations[26]. Such points experience locally asymmetric electric fields due to surrounding electronic clouds. At a molecular level, these fields are weak and stochastic; they do not allow one to observe chirotopic effects in the macroscale and in the far field. In fact, it was thought to be impossible to observe such effects for molecules, polymers or crystals. The situation changes, however, at the nanoscale level because the strong local symmetry-broken fields can be generated by achiral photons in resonance with nanostructures. A half of photonic elements can be selectively excited, producing, for instance, left-handed chirotopic field depending on the incident polarization. The other half, producing the right-handed chirotopic field, can remain predominantly silent. Consequently, the helicity of photons emitted from such materials becomes symmetry broken, although luminophores in them remain achiral, randomly oriented and non-dichroic.

As a proof of principle, we demonstrate CPL emission from both upconverting nanoparticles (NPs) and downshifting dye molecules localized at chirotopic sites on achiral nanostructures. Selective excitation of luminophores at chirotopic sites with linearly polarized pump light enables a widely tunable chiroptical response, with g_{lum} spanning −1.58 to 1.65 and thus approaching the dissymmetry limit (i.e., −2 to 2) for a tunable CPL source.

Results

Local symmetry breaking and nanoscale chirotopicity

Following the treatment of chirotopic geometries by Mislow[26,27], let us first consider an array of achiral nanogroove dimers in a gold film, depicted in Fig. 1a. Although it globally possesses a mirror symmetry of σ_1, all the sites in the model (e.g., Points 1, 2), except for those lying in the σ_1 plane (e.g., Points 3, 4), are characterized to be chirotopic or, by other words, locally chiral. Distinguished from the concept of chirality, which is purely geometric and binary, chirotopicity implies a locally asymmetric environment that can be assessed and potentially engineered for any point in a gradual manner using chirality measures[23]. At the molecular level, the chirotopic effect is too weak to induce strong circularly polarized light emission due to the size mismatch between molecules and light wavelengths. In contrast, local symmetry breaking should be particularly stronger in resonant nanostructures (i.e., meta-atoms) with large polarizability, where the locally enhanced electric fields associated with optical resonances take the role of the electronic wavefunctions of atoms. For measuring optical chirotopicity, local circular dichroism (LoCD) is defined as:

$$\mathrm{LoCD}(\mathbf{r}) = \frac{|\mathbf{E}_{RCP}(\mathbf{r})|^2 - |\mathbf{E}_{LCP}(\mathbf{r})|^2}{|\mathbf{E}_{RCP}(\mathbf{r})|^2 + |\mathbf{E}_{LCP}(\mathbf{r})|^2} \quad (1)$$

where electric field intensities $|\mathbf{E}_{RCP}(\mathbf{r})|^2$ and $|\mathbf{E}_{LCP}(\mathbf{r})|^2$ are obtained under normal incidence of right- and left-handed circularly polarized (RCP and LCP) light. The LoCD map calculated for the plasmonic nanodimer is zero on the σ_1 plane due to the existence of local symmetry (Fig. 1b). Besides, since LoCD is a parity-odd scalar, it is forced to have opposite values on the two sides of the symmetric plane σ_1, which will cancel each other in the far field to manifest no circular dichroism in scattering. If rectangular nanogrooves with higher symmetry are considered (Fig. 1c), more complex LoCD distributions are presented with alternating regions of positive and negative values. For the cases of chiral Z-shaped or fan-shaped nanogrooves (Fig. 1c), positive and negative LoCD values are no longer balanced, resulting in non-zero circular dichroism scattering signals in the far field. In fact, almost all types of nanostructures exhibit local symmetry breaking, with the only exception of an isotropic circular disk. Experimentally, the existence of chirotopic centers in NPs with reduced global symmetry can be vividly observed via their light-induced growth due to locally asymmetric plasmonic fields[28,29]. We note that another quantity, i.e., optical chirality C, is also utilized for measuring the chirality of near fields[30], but it differs from LoCD in both physical meaning and applicable scenarios (see details in Supplementary Note 1).

Although LoCD, by definition, is related to differential absorption of CPL, it may also enable chiral light emission according to Lorentz Reciprocity. If a photon emitter is selectively located at those chirotopic sites with positive (or negative) LoCD values, RCP (or LCP) light will be emitted. This can be validated by electromagnetic simulations of local emission dissymmetry factor $g_{lum}(\mathbf{r})$ map (Fig. 1b), taking advantage of its relationship to LoCD($\mathbf{r}$) as (see Supplementary Note 2):

$$g_{lum}(\mathbf{r}) = 2 \cdot \mathrm{LoCD}(\mathbf{r}) \quad (2)$$

where $g_{lum}(\mathbf{r})$ is defined as $g_{lum}(\mathbf{r}) = 2\cdot(I_{RCP} - I_{LCP})/(I_{RCP} + I_{LCP})$ and evaluated for a local emitter, while I_{RCP} and I_{LCP} are the RCP and LCP components of emitted light. $g_{lum}(\mathbf{r})$ values approaching the theoretical maximum of 2 are observed in Fig. 1b.

Although chirotopicity is universally present in nanostructures of virtually any shape, certain principles have to be obeyed in structural designs in order to harness nanoscale chirotopicity as a generalizable method for enabling high-intensity, high-g_{lum} chiral emission. First, the LoCD amplitudes should be increased to boost emission ellipticity $g_{lum}(\mathbf{r})$. Second, the LoCD regions of opposite polarity should be spatially separated in order that they can be selectively addressed without crosstalk. Third, regions with large LoCD and strong electric fields should be overlapped so that the chiral emission intensity is enhanced as well. According to these design principles, nanostructures with lower symmetry are preferred, which can be inferred by comparing the LoCD maps of plasmonic dimers and nanorectangles (Fig. 1b, c). Meanwhile, chiral nanostructures are not desired because their LoCD patterns tend to be twisted (Fig. 1c). Their uneven distributions of positive and negative LoCD further hinder the identification of true chirotopic effects on g_{lum}. Therefore, achiral nanostructures with only one mirror plane are ideal candidates for enabling chiral emission from chirotopic sites, e.g., the plasmonic dimer in Fig. 1a.

Chirotopic designs for circularly polarized light emission

We utilize the nanogroove dimer design for generating circularly polarized light emission from the chirotopic effect. Lanthanide-doped upconversion NPs (UCNPs) are adopted as achiral luminophores, which exhibit a photoluminescence (PL) band at around 660 nm when pumped at 980 nm, showing no luminescence chirality (see Methods). SEM images of the nanodimer array with and without UCNPs are depicted in Fig. 1a. As a result of near-field coupling between adjacent nanogrooves (see Supplementary Fig. 6), the nanodimer array supports an antisymmetric and a symmetric plasmonic mode ($\mathbf{E}_{sym}$ or $\mathbf{E}_{anti}$) with respect to the mirror plane, which is clearly observed in the simulated and experimental reflection spectra (Fig. 2a). Their corresponding near-field distributions are plotted in Fig. 2b. Non-zero LoCD can only be induced when the two modes are simultaneously excited and interfere (see Supplementary Note 3), whose amplitude is derived

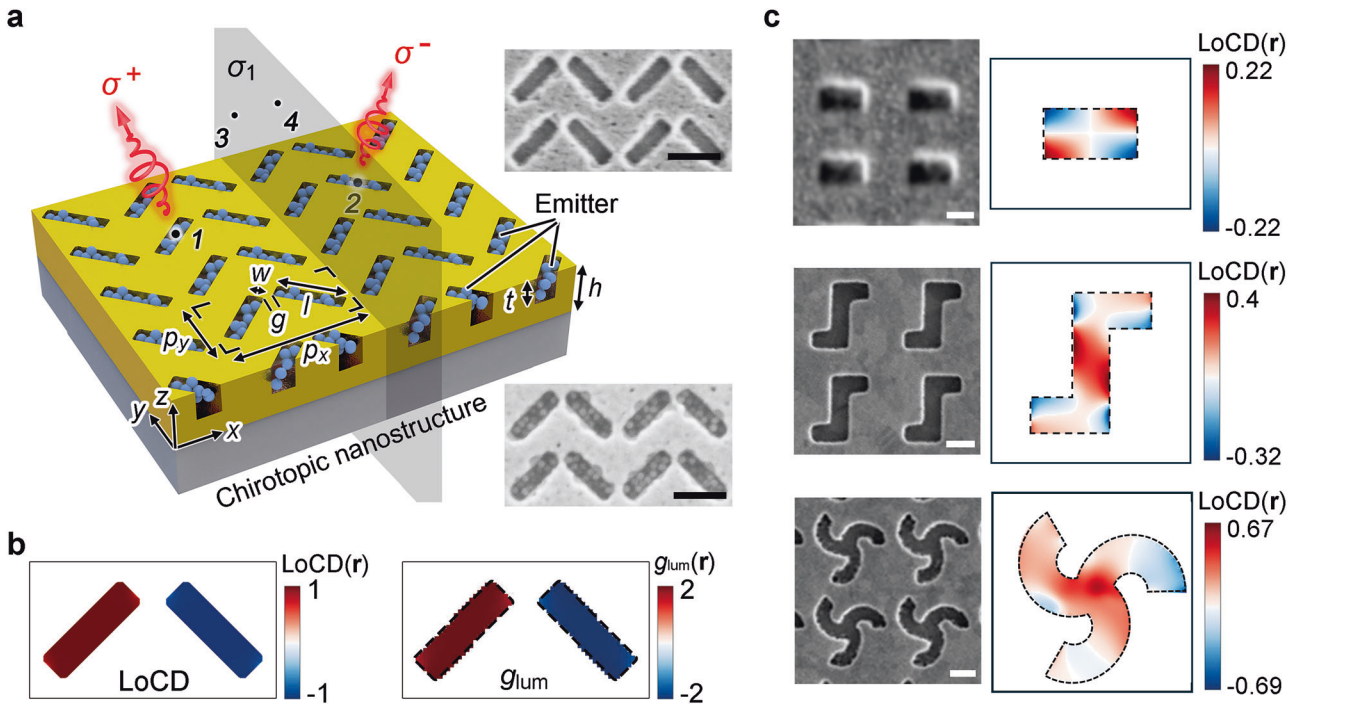

Fig. 1 | Fundamental principles of nanoscale chirotopicity. a Schematic of a plasmonic chirotopic device enabling circularly polarized emission from achiral emitters. The structural parameters are: $p_x = 382$ nm, $p_y = 210$ nm, $l = 175$ nm, $w = 50$ nm, $g = 40$ nm, $h = 160$ nm, and $t = 70$ nm. SEM images of the device with (bottom) and without (top) UCNPs are shown on the right. Scale bar, 200 nm. **b** Calculated LoCD(**r**) and g_{lum}(**r**) distributions of the plasmonic nanogroove dimer, exhibiting large optical chirotopicity at the wavelength of 660 nm. **c** SEM images and calculated LoCD(**r**) distributions for the plasmonic rectangular, Z-shaped, and fan-shaped nanogrooves at the wavelength of 660 nm. The plot ranges of LoCD are 640 nm × 480 nm, 650 nm × 650 nm, and 650 nm × 650 nm from top to bottom. Scale bar, 200 nm.

as:

$$\mathrm{LoCD}(\mathbf{r}) = \frac{2 \cdot \sin(\varphi) \cdot \left|\mathbf{E}_{\mathrm{sym}}(\mathbf{r})\right| \cdot \left|\mathbf{E}_{\mathrm{anti}}(\mathbf{r})\right|}{\left|\mathbf{E}_{\mathrm{sym}}(\mathbf{r})\right|^2 + \left|\mathbf{E}_{\mathrm{anti}}(\mathbf{r})\right|^2} \tag{3}$$

where φ is the phase difference between the two modes. To obtain strong LoCD over large areas, the excited symmetric and antisymmetric modes should have similar mode profiles and be equally excited with a phase delay of π/2 or 3π/2. In our design, the two modes indeed have similar intensities and a phase delay of about 3π/2 at the wavelength around 660 nm, overlapping with the emission band of UCNPs (see Supplementary Fig. 7a). All design principles are thus satisfied, and LoCD values above 0.97 and below −0.97 are achieved over the left and right nanogrooves (Fig. 1b). As a result, the near fields are highly enhanced and localized at the left (or right) nanogroove for RCP (or LCP) incidence at 660 nm (Fig. 2c).

To harness such strong chirotopicity for circularly polarized light emission, one needs to selectively place luminophores at those chirotopic sites with positive or negative LoCD. This task is, however, far from being simple for current fabrication techniques, because NPs are almost equally deposited in the two nanogrooves with opposite LoCD (Fig. 1a). An alternative solution is to excite luminophores in only one nanogroove. Aiming at the fundamental proof of concept for the possibility of chiral emission from achiral materials via local symmetry breaking, we employ linearly polarized laser beam at 980 nm and control its orientation angle θ. Then, the left nanogroove can be individually addressed for $\theta = 135°$ (Fig. 2d). Electric field intensity integrated over the left nanogroove (Σ_{LG}) is calculated to be 15 times stronger than the right one (Σ_{RG}), showing a large linear polarization selectivity at this wavelength (see Supplementary Fig. 8). Then, UCNPs contained in the left nanogroove are pumped to excited states and undergo non-radiative energy transfer from electrons to the chirotopic plasmonic mode at 660 nm, resulting in RCP upconversion luminescence. For the case of $\theta = 45°$, the right nanogroove is selectively excited to generate LCP luminescence. The g_{lum} value of the device can be theoretically predicted as:

$$g_{\mathrm{lum}} = \frac{\iiint_V g_{\mathrm{lum}}(\mathbf{r})\left|\mathbf{E}(\mathbf{r})\right|^2 \mathrm{d}\mathbf{r}}{\iiint_V \left|\mathbf{E}(\mathbf{r})\right|^2 \mathrm{d}\mathbf{r}} = \frac{2\iiint_V \mathrm{LoCD}(\mathbf{r})\left|\mathbf{E}(\mathbf{r})\right|^2 \mathrm{d}\mathbf{r}}{\iiint_V \left|\mathbf{E}(\mathbf{r})\right|^2 \mathrm{d}\mathbf{r}} \tag{4}$$

where **E**(**r**) is evaluated for the pump wavelength of 980 nm, g_{lum}(**r**) and LoCD(**r**) are dependent on the luminescence wavelength. The volume integration is conducted over the two nanogrooves where UCNPs are present. As shown in Fig. 2e, the g_{lum} spectrum is calculated to be resonant at 660 nm with peak values of up to 1.8 and −1.8 for $\theta = 135°$ and 45°. But for $\theta = 90°$, the g_{lum} spectrum maintains zero.

We compare the nanogroove dimer structure with rectangular, Z-shaped and fan-shaped nanogrooves, in terms of predicted g_{lum} spectrum (Supplementary Fig. 9). Since regions of positive and negative LoCD are usually intermixed in space for the three alternative structures, making them hard to excite selectively, their predicted g_{lum} values are much smaller than nanogroove dimers (Supplementary Fig. 9). Moreover, we note that our chirotopic design is very robust against the incident angle of pump light. The peak value and spectral position of g_{lum} remain almost unchanged over a wide range of incident angles (Supplementary Fig. 10). As a fundamental phenomenon in optics, spin-orbit coupling has been extensively investigated for directional excitation of surface plasmon polaritons[31] and guided modes[32], as well as selective coupling of circular dipoles[33–35]. In these works, spin-polarized excitation sources, either far-field circularly polarized light or near-field circular dipoles, are directionally coupled to distinct modes. Our work represents an application of spin-orbit

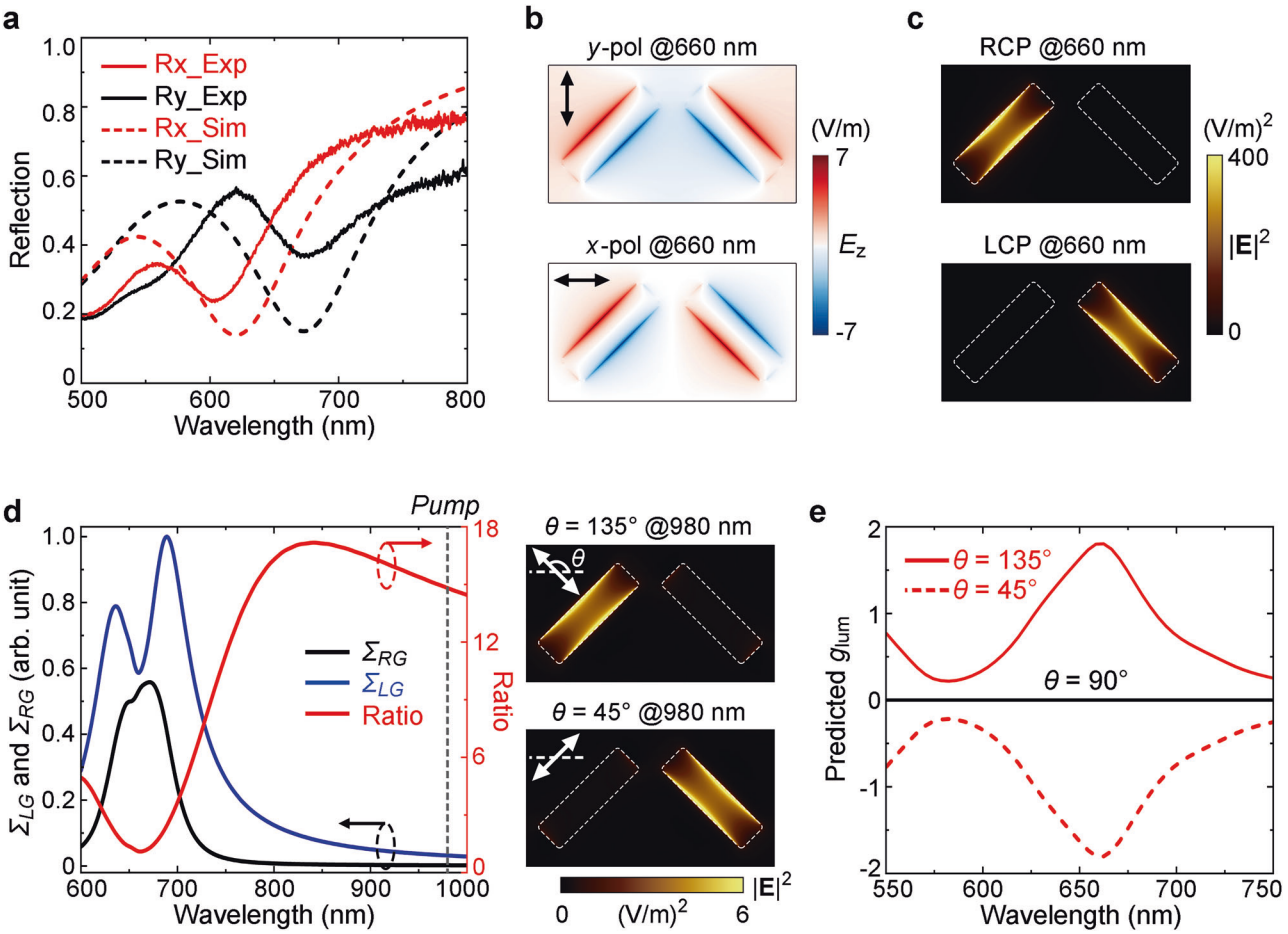

Fig. 2 | Chirotopic design for circularly polarized light emission. a Simulated and measured reflection spectra of the device under *x*- and *y*-polarized illuminations. **b** E_z distributions of symmetric and antisymmetric modes at 660 nm. **c** $|\mathbf{E}|^2$ distributions under RCP (middle) and LCP (bottom) incidence. **d** Volume-integrated electric intensities over the left and right nanogroove (Σ_{LG} and Σ_{RG}), along with their ratio (Σ_{LG}/Σ_{RG}), under linearly polarized incidence of $\theta = 135°$. Electric field distributions at 980 nm for the cases of $\theta = 135°$ and 45° are shown on the right. **e** Theoretically predicted g_{lum} spectra of the device for the pump orientations of $\theta = 45°$, 90° and 135°.

coupling, where achiral emitters at different locations generate free-space chiral emission with opposite handedness.

Experimental results for chirotopic upconversion luminescence

To experimentally investigate the emission properties of our chirotopic device, a 980-nm continuous-wave laser with a power of 30 mW is passed through a linear polarizer, a half-wave plate, and then normally illuminated on the device. The upconversion luminescence is collected with the same objective and analyzed (see Methods). When the orientation angle of the pump light θ is set to 135°, g_{lum} is measured to be larger than 1.55 over the whole emission band from 645 nm to 670 nm. The maximum g_{lum} of 1.65 is acquired at around 660 nm (Fig. 3a), which matches our predicted value. Meanwhile, the PL intensity is as high as 70 times stronger than the reference case with UCNPs deposited on a bare gold film (Supplementary Fig. 11). Once the orientation angle θ is switched to 45°, the retrieved g_{lum} is reversed to −1.58 (Fig. 3b). Further, if θ is set to 90°, a negligibly small g_{lum} is obtained over the emission band (Fig. 3c). By controlling θ, the g_{lum} can be continuously tuned between 1.65 and −1.58, approximately following the relationship $g_{lum} = -1.64 \cdot \sin(2\theta)$ (Fig. 3d, Supplementary Fig. 12). To the best of our knowledge, this is the largest tuning range ever realized for compact CPL emitters[2–5]. We also measure the g_{lum} of upconverted luminescence as a function of θ for the rectangular, Z-shaped and fan-shaped nanogroove samples (Supplementary Fig. 13). As theoretically predicted before, both the peak values and tuning ranges of g_{lum} are much smaller than the nanogroove dimer design. For passive metasurfaces operating in the elastic scattering regime, the interaction preserves the coherence between the incident and scattered fields, meaning the scattered light retains a deterministic phase relationship and well-defined polarization state relative to the incident wave. Thus, it is straightforward and easy to manipulate scattered polarization and phase with nanostructures. In contrast, inelastic scattering involves energy exchange (e.g., with molecular vibrations or electronic excitations), leading to nonlinear and often stochastic responses. The scattering process is largely insensitive to the phase of the incident field, and the emission polarization is primarily determined by the metasurface eigenmodes at the emission wavelength and is typically fixed once the metasurface is fabricated[11–14]; making substantial post-fabrication control of emission chirality challenging.

If the measured PL polarizations are mapped on a Poincaré sphere (Fig. 3e), they follow a trajectory from near the north pole to near the south pole, approaching the performance limit of a tunable CPL source. The polar diagrams of polarizations for the cases of $\theta = 45°$ and 135° show typical circular polarization patterns (Fig. 3e). But for the cases of $\theta = 0°$ and 90° with $g_{lum} = 0$, the polar diagrams correspond not to linear polarizations, but to unpolarized emission resulting from incoherent superposition of equivalent RCP and LCP components, because UCNPs in the left and right nanogrooves are equally excited (Fig. 3e). Further, we experimentally examine the dependence of

https://doi.org/10.1038/s41467-026-74088-8

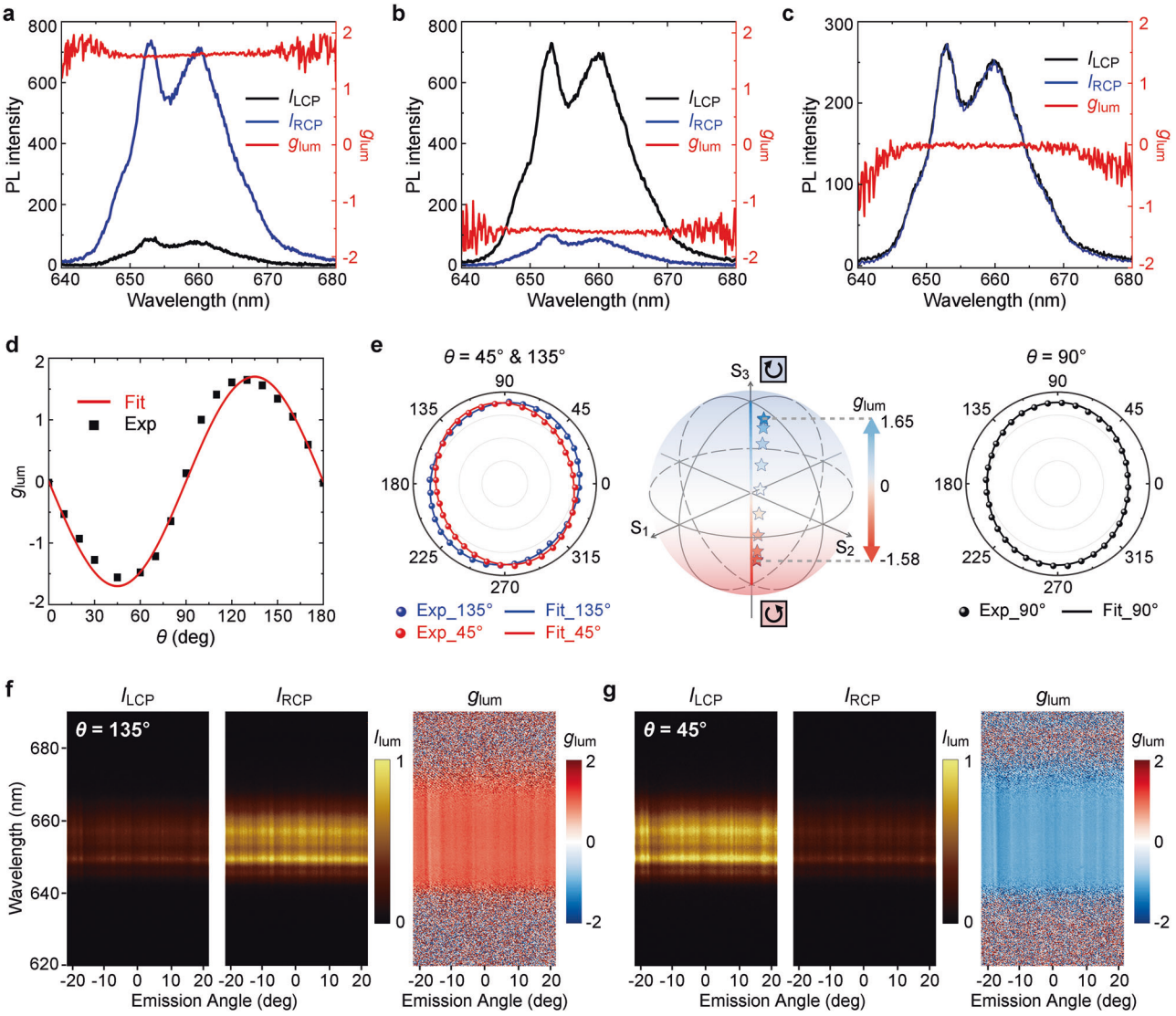

Fig. 3 | Experimental results for chirotopic upconversion luminescence. **a**–**c** Helicity-resolved PL intensity and g_{lum} spectra measured for pump polarization angles of θ = **a** 135°, **b** 45°, and **c** 90°. **d** Dependence of experimental g_{lum} values on the polarization angle θ, fitted with a sine function. **e** Evolution of measured luminescence polarizations is mapped on a Poincaré sphere, represented by colored stars. The polar diagrams of polarizations for θ = 45°, 135° and θ = 90° are plotted on the two sides. **f**, **g** Helicity-resolved PL intensity and g_{lum} spectra measured with respect to the emission angle for θ = **f** 135° and **g** 45°.

emission properties on emission angles. The emission intensities exhibit an advantageous flat band in the momentum space (Fig. 3f and g), while the g_{lum} spectra display high values for θ = 135° and 45° over a wide angular range, excluding the possible impact of extrinsic chirality corroborated by the experimental data of θ = 0° and 90° (Supplementary Fig. 14). In sharp contrast, most of the existing CPL emitters based on intrinsically or extrinsically chiral metasurfaces can only achieve high g_{lum} values over a severely limited range of angles[10–20], which endows chirotopic devices with advantages in angular tolerance.

Dynamic chirotopic downshifting luminescence

To further validate the concept and demonstrate the advantages of harnessing emission from globally achiral structures with nanoscale chirotopic electromagnetic fields, we test luminescence of 4-(dicyanomethylene)−2-methyl-6-(4-dimethylaminostyryl)−4H-pyran (DCM) dyes deposited onto chirotopic sites (Fig. 4a). For reference, a bare DCM-doped PMMA film on glass has achiral broadband emission centered at 635 nm, when pumped at 520 nm (Fig. 4b). If a 70 nm-thick DCM-doped PMMA film is deposited on the plasmonic nanodimer array, an antisymmetric and a symmetric mode are observed at 577 nm and 641 nm (Fig. 4b), resulting in the maximum chirotopicity achieved within the emission band of DCM. Then, a 520-nm linearly polarized pump light with θ = 135° leads to a g_{lum} as high as 1.24 (Fig. 4c). By controlling the orientation angle θ, the g_{lum} value can be continuously tuned between 1.24 and −1.08 (Fig. 4c, Supplementary Fig. 15), approximately following the relationship $g_{lum} = -1.16 \cdot \sin(2\theta)$ as observed above for UCNPs. We note that the magnitude of g_{lum} for DCM is smaller than that for UCNPs, because DCM is also deposited outside nanogrooves, where the chirotopicity is weaker than inside them (Supplementary Fig. 16).

The broad emission band of DCM helps uncover how the spectral dependence of the giant g_{lum} originates from the chirotopic effect, which is difficult to observe with the narrow-band emission of UCNPs. As shown in Fig. 4d, the g_{lum} spectrum of Sample 1 exhibits a strong resonance at 610 nm, where the spectral lines of antisymmetric and symmetric modes of the plasmonic nanostructures are intersected to fulfill the criteria in Eq. (3). By tailoring the spectral positions of the two modes through structural designs, we can customize the g_{lum} resonance to a specific wavelength. As demonstrated in Fig. 4d, the helicity-

https://doi.org/10.1038/s41467-026-74088-8

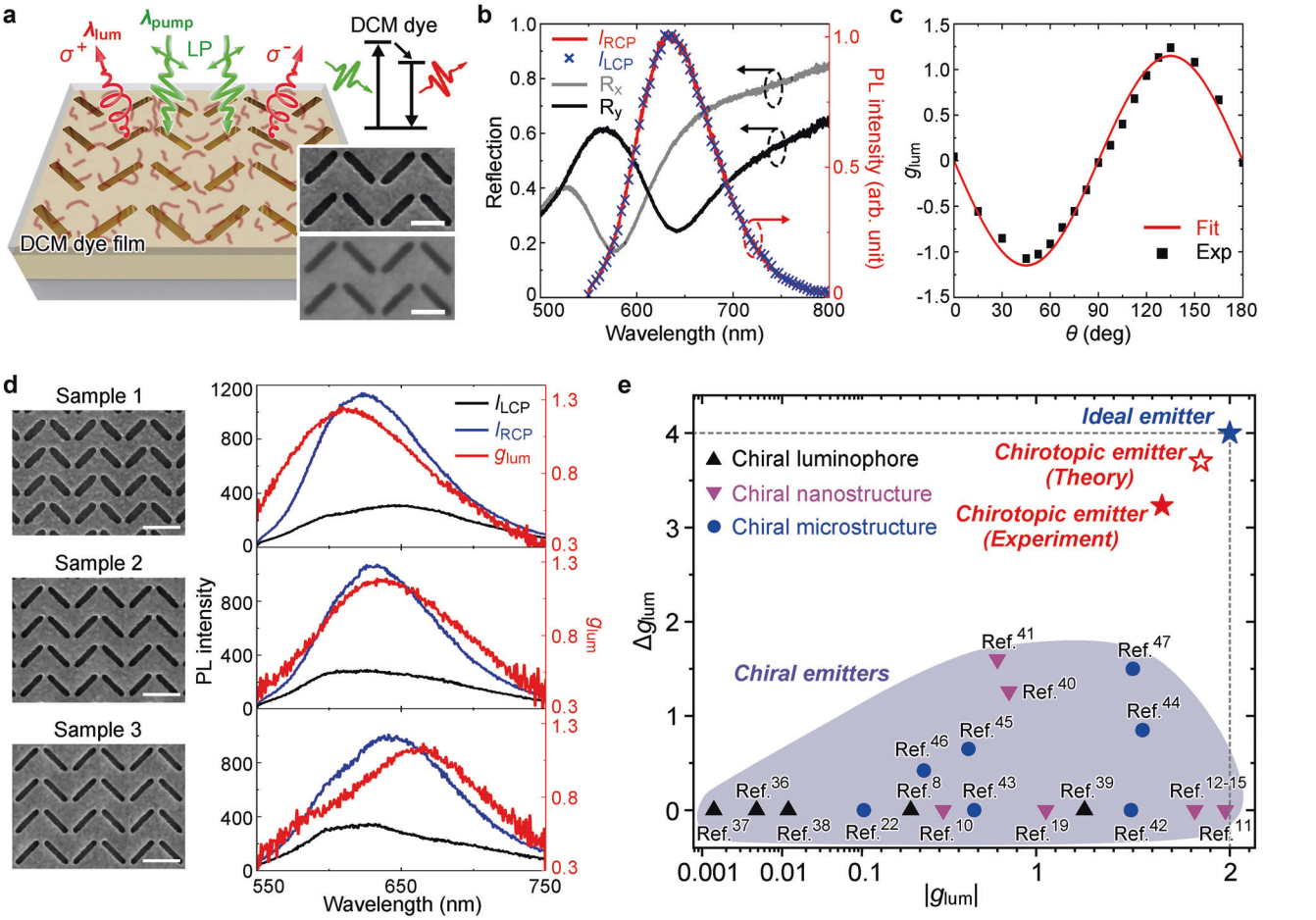

Fig. 4 | Tunable chirotopic luminescence and comparative performances of CPL emitters. a Schematic of a plasmonic chirotopic device for achieving chirality-tunable luminescence from DCM dyes. SEM images of the nanogroove dimer with (bottom) and without (top) a DCM film are depicted on the right. Scale bar: 200 nm. **b** Experimental reflection spectra of the device under *x*- and *y*-polarized illuminations, together with the helicity-resolved PL spectra of a bare DCM-doped PMMA film pumped at 520 nm. **c** Dependence of the measured g_{lum} values on the polarization angle θ, fitted with a sine function. **d** Helicity-resolved PL intensity and g_{lum} spectra for different chirotopic devices at $\theta = 135°$. Their SEM images are shown on the left. Scale bar: 300 nm. **e** Comparison of chiral dissymmetry parameters for chirotopic emitters and other CPL emitters: $|g_{lum}|$ vs Δg_{lum}. A log scale is utilized for the $|g_{lum}|$ due to a wide range from 0.001 to 0.1.

resolved PL spectra are significantly modulated with the resonance wavelength of g_{lum} redshifted from Sample 1 to 3 (Supplementary Fig. 17).

Comparison with chiral emitters

One can compare our chirotopic nanostructure emitters with some typical chiral emitters in terms of two key metrics: the maximum value of emission dissymmetry factor $|g_{lum}|$ and its tuning range Δg_{lum} (Fig. 4e). Most chiral organic molecules have rather low $|g_{lum}|$, typically on the order of 10^{-5} to 10^{-2}, because their magnetic transition dipole moments are much smaller than their electric dipole moments[36–38]. Although inorganic crystals[8] and lanthanide complexes[39] can enable larger $|g_{lum}|$ than chiral organic molecules, their circularly polarized luminescence is difficult to tune for specific emission due to quantum mechanical constraints. Given these challenges, chiral nanostructures, particularly in the form of planar arrays known as chiral metasurfaces, have offered an alternative route to realizing compact CPL sources with large g_{lum} and strong luminescence intensity[10–20]. Such nanostructure-based CPL emitters are generally designed to exhibit either intrinsic chirality through three-dimensional mirror-asymmetric geometries[10–13,16–18] or extrinsic chirality via slant-angle emission configurations[14,15,19,20]. The recent adoption of chiral bound state in the continuum[11–14] has further pushed the experimental $|g_{lum}|$ values beyond 1.8, approaching the theoretical limit of 2. Nevertheless, intrinsic chiral bound states in the continuum nanostructures usually demand specialized and elaborate nanofabrication techniques, such as slanted reactive ion etching[11,12] and grayscale electron beam lithography[13], whereas slant-angle emission schemes suffer from strict alignment requirements, inherent instability, and integration challenges. Moreover, post-fabrication tunability of the g_{lum} is still a dilemma for the existing chiral nanostructure emitters[10–20]. Exploiting spin-locked transition metal dichalcogenides presents a possible solution to dynamically modulate g_{lum}[40,41], but their ultrathin thickness limits emission intensities, and the achieved $|g_{lum}|$ and Δg_{lum} values remain moderate. As to circularly polarized emission assisted by helical microstructures[22,42–47], it typically requires considerable thicknesses to accumulate $|g_{lum}|$ and involves complicated structures to accommodate external stimuli.

By contrast, our proposed chirotopic nanostructure emitter does not rely on intrinsically or extrinsically chiral nanostructures, but instead on the selective excitation of luminophores at specific chirotopic sites. Compared to chiral metasurfaces employing bound states in the continuum[11–14]—which excel in achieving higher $|g_{lum}|$ values, supporting polarization-insensitive excitation, and producing stronger Purcell effects due to their larger quality factors—the chirotopic emitter offers a larger tuning range Δg_{lum}. Moreover, it utilizes planar achiral nanostructures that are compatible with conventional nanofabrication techniques, and generates chiral emission in the normal

direction with robust angular tolerance. Therefore, neither approach is universally superior; the choice should be made based on the specific application scenario.

Discussion

Motivated by the theoretical framework of chirotopicity that remained unproven for 50+ years, we show that local nanoscale chirality of globally achiral materials can produce CPL with both high intensity and ellipticity. Symmetry restrictions imposed on electronic states of luminophores to emit circularly polarized photons have been removed. The observed effect, driven by local symmetry breaking and electromagnetic field asymmetry, is generalizable to a wide range of luminophores, inclusive of NPs and organic dyes, which is particularly significant in the context of g_{lum} values approaching the theoretical maximum. Extension of the framework of chirotopic field-matter interactions should encompass its implications for nonlinear optics.

Future translational studies should include the selective placement of emitters at chirotopic sites, which would eliminate the requirement for specific excitation polarization and could further promise electrically-pumped chiral light-emitting devices. However, since chirotopic sites are distributed at deep-subwavelength scales (~10 nm), achieving such selective placement imposes high demands on positioning resolution, accuracy, and stability. Aligned electron beam lithography represents a viable high-resolution approach[48], yet it relies on extremely precise alignment, is costly, and remains difficult to scale. In contrast, plasmon-induced selective exposure offers a potentially low-cost, fast alternative[49,50]. However, it depends heavily on sophisticated nanostructure designs and accurate control of exposure dosage, and typically provides lower positioning resolution and accuracy compared to electron beam lithography, thereby limiting the achievable g_{lum}. Overall, current schemes remain largely proof-of-principle, and the large-scale, selective addressing of nanoscale chirotopicity for integrating into scalable devices still poses significant technological hurdles. Despite these challenges, the chiral emission scheme based on nanoscale chirotopicity proposed here holds potential for applications in polarization-encoded displays, enantioselective sensors, and compact CPL sources.

Methods

Synthesis of UCNPs

In a 100 ml three-neck round-bottom flask, 1.36 mmol $Y(CH_3COO)_3{\bullet}xH_2O$, 0.6 mmol $Yb(CH_3COO)_3{\bullet}xH_2O$, 0.04 mmol $Er(CH_3COO)_3{\bullet}xH_2O$, 30 ml octadecene and 12 ml oleic acid are mixed under stirring at the speed of 800 rpm. Then, the mixed solution is heated to 120 °C in a vacuum for 15 min. After that, the solution temperature is cooled to 50 °C under an Ar flow (20 ml/min). Then, 8.0 mmol ammonium fluoride and 5.0 mmol sodium hydroxide in methanol (20 ml) solution are added to the flask under stirring for half an hour. After 30 min, the solution temperature is raised to 70 °C to remove the residual methanol under vacuum. Subsequently, the solution temperature is gradually increased to 300 °C at a rate of 20 °C per minute. The reaction system is kept for 90 min to ensure the growth of $NaYF_4$:30%Yb,2%Er crystals completely. Finally, the solution is cooled to 25 °C naturally. The final brown solution is precipitated by 80 ml of ethanol first. The NPs are isolated at a centrifugation speed of 4193 g. The resulting pellets are washed three times with 10 ml hexane and 20 ml ethanol alternately. The final product is dispersed in 8 mL of hexane for the second step, coating the $NaYbF_4$ shell.

The coating process of $NaYbF_4$ shell on $NaYF_4$:30%Yb,2%Er is similar to the above core synthesis process. Typically, in a 100 ml three-neck round-bottom flask, 2.0 mmol $Yb(CH_3COO)_3{\bullet}xH_2O$, 30 ml octadecene and 12 ml oleic acid are added under stirring at the speed of 800 rpm. Then, the solution temperature is increased to 120 °C under vacuum. 15 min later, the solution temperature is cooled to 50 °C under an Ar flow (20 ml/min). Subsequently, $NaYF_4$:30%Yb,2%Er NPs synthesized in the first step, followed by 8.0 mmol ammonium fluoride and 5.0 mmol sodium hydroxide in methanol, are added to the flask with stirring for 30 min at a speed of 800 rpm. After that, the solution temperature is raised to 70 °C to remove the methanol under vacuum. After the methanol is removed completely, the solution temperature is increased to 300 °C quickly at the speed of 20 °C per minute and kept for 90 min to ensure the growth of $NaYF_4$:30%Yb,2% Er@$NaYbF_4$ crystals completely. Finally, the solution is cooled to 25 °C naturally. The final brown solution is precipitated by 80 mL ethanol firstly and isolated at a centrifugation speed of 4193 g. The resulting pellets are washed three times with 10 mL hexane and 20 ml ethanol alternately. The final product is dispersed in 8 mL of hexane for the third step, the standby coating of the $NaYF_4$ inert shell. The average size of NP is determined as 27 nm, measured by transmission electron microscopy (Supplementary Fig. 1a). When pumped at 980 nm. A characterized photoluminescence (PL) band is exhibited at around 660 nm with no luminescence chirality (Supplementary Fig. 1b), due to the intrinsic crystal lattice symmetry.

Fabrication of our chirotopic device

The fabrication process of our device is illustrated in Supplementary Fig. 2. Firstly, a cleaned silicon wafer is spin-coated with high-resolution electron beam resist HSQ (2 wt% in methyl isobutyl ketone, Dow Coming XR-1541) and patterned by electron beam lithography (JEOL-6300FS, acceleration voltage: 100 kV). Secondly, the HSQ pattern is transferred to the underlying silicon substrate by inductively coupled plasma etching (Oxford PlasmaSystem100 ICP380) with a combination of SF_6 and C_4F_8 gases (ICP power: 1300 W, RF power: 50 W, temp: 10 °C), with the height of silicon pillars precisely controlled by the etching time. The HSQ mask is then removed by wet etching (BOE). Thirdly, a gold film with a thickness of 160 nm is deposited on the silicon substrate by an electron beam evaporator (AdNaNotek EBS-150). Then, a glass slide is adhered to the surface of the gold film using the optical adhesive OA glue (Norland Products NOA61) and fixed with ultra-violet radiation after curing. Finally, gold nanogrooves on the glass slide are stripped from the silicon substrate.

For the deposition of UCNPs, a solution containing UCNPs at a concentration of 1 mg/ml is sonicated for 1 min to fully disperse the NPs. Then, a 100 µL UCNPs solution is mixed with 1200 µL n-hexane to dilute the concentration. Subsequently, the sample is placed flat in the solution, with the sample surface slightly lower than the liquid surface, and sonicated for 1 min. Finally, the sample is taken out and dried naturally. For the deposition of the DCM-doped PMMA film, a 70 nm DCM-doped PMMA film (mass ratio 1:240) is spin-coated for 40 s at a speed of 6000 rpm.

Numerical simulations

All simulations in this work are performed using a finite-element-method solver (COMSOL Multiphysics). The permittivity of gold is set based on Johnson and Christy data, while the refractive index of UCNPs and DCM-doped PMMA film is set as 1.45. Periodic boundary conditions are employed in the x- and y-directions, and perfectly matched layers are utilized in the z-direction. When calculating the local dissymmetry factor of luminescence $g_{lum}(\mathbf{r})$, an electric dipole with a certain orientation is swept over the near field of nanostructures, while the circular polarization of the radiative field is analyzed.

Optical characterizations

As shown in Supplementary Fig. 3, for the measurement of upconversion luminescence, a CW laser at 980 nm is passed through a linear polarizer and a half-wave plate and then focused on the chirotopic device sample using a 20 × objective (NA = 0.4). The upconversion luminescence is collected with the same objective, passed through a low-pass filter to eliminate the influence of pump light, and finally directed to a spectrometer (Horiba, iHR 320). Circular polarization is

examined using a combination of a quarter-wave plate and a linear polarizer. To measure downshifting luminescence, the wavelength of the CW laser is changed to 520 nm, while the low-pass filter is replaced by a long-pass filter. All beam splitters utilized are polarization-maintaining.

Data availability

All data needed to evaluate the conclusions in this paper are available in the main text or the supplementary materials. The source data file has been deposited in Figshare under the accession code DOI link[51].

References

1. Barron, L.D. Molecular light scattering and optical activity. (Cambridge University Press, 2009).
2. Zhang, Y. et al. Circularly polarized luminescence in chiral materials. *Matter* **5**, 837–875 (2022).
3. Furlan, F. et al. Chiral materials and mechanisms for circularly polarized light-emitting diodes. *Nat. Photonics* **18**, 658–668 (2024).
4. Deng, Y. et al. Circularly polarized luminescence from organic micro-/nano-structures. *Light.: Sci. Appl.* **10**, 76 (2021).
5. Jiang, S. & Kotov, N. A. Circular polarized light emission in chiral inorganic nanomaterials. *Adv. Mater.* **35**, 2108431 (2023).
6. Sawada, Y. et al. Rhodium-catalyzed enantioselective synthesis, crystal structures, and photophysical properties of helically chiral 1, 1′-bitriphenylenes. *J. Am. Chem. Soc.* **134**, 4080–4083 (2012).
7. Yang, S., Zhang, S., Hu, F., Han, J. & Li, F. Circularly polarized luminescence polymers: from design to applications. *Coord. Chem. Rev.* **485**, 215116 (2023).
8. Ma, J. et al. Chiral 2D perovskites with a high degree of circularly polarized photoluminescence. *ACS Nano* **13**, 3659–3665 (2019).
9. Lu, J., Jung, H. J., Kim, J.-Y. & Kotov, N. A. Bright, circularly polarized black-body radiation from twisted nanocarbon filaments. *Science* **386**, 1400–1404 (2024).
10. Konishi, K. et al. Circularly polarized light emission from semiconductor planar chiral nanostructures. *Phys. Rev. Lett.* **106**, 057402 (2011).
11. Zhang, X., Liu, Y., Han, J., Kivshar, Y. & Song, Q. Chiral emission from resonant metasurfaces. *Science* **377**, 1215–1218 (2022).
12. Chen, Y. et al. Observation of intrinsic chiral bound states in the continuum. *Nature* **613**, 474–478 (2023).
13. Lim, Y. et al. Maximally chiral emission via chiral quasibound states in the continuum. *Laser Photonics Rev.* **17**, 2200611 (2023).
14. Chen, Y. et al. Compact spin-valley-locked perovskite emission. *Nat. Mater.* **22**, 1065–1070 (2023).
15. Rong, K. et al. Spin-valley Rashba monolayer laser. *Nat. Mater.* **22**, 1085–1093 (2023).
16. Kan, Y. et al. Metasurface-enabled generation of circularly polarized single photons. *Adv. Mater.* **32**, 1907832 (2020).
17. Lu, X., Tan, Y., Gao, Z. & Ding, T. Deterministic placement of achiral emitters in superchiral fields for superior chiral photoluminescence. *Nano Lett.* **25**, 7137–7143 (2025).
18. Le, K. Q., Hashiyada, S., Kondo, M. & Okamoto, H. Circularly polarized photoluminescence from achiral dye molecules induced by plasmonic two-dimensional chiral nanostructures. *J. Phys. Chem. C.* **122**, 24924–24932 (2018).
19. Seo, I. C. et al. Circularly polarized emission from organic-inorganic hybrid perovskites via chiral Fano resonances. *ACS Nano* **15**, 13781–13793 (2021).
20. Tian, J. et al. Optical Rashba effect in a light-emitting perovskite metasurface. *Adv. Mater.* **34**, 2109157 (2022).
21. Albano, G., Pescitelli, G. & Di Bari, L. Reciprocal and non-reciprocal chiroptical features in thin films of organic dyes. *ChemNanoMat* **8**, e202200219 (2022).
22. Lu, J. et al. Nano-achiral complex composites for extreme polarization optics. *Nature* **630**, 860–865 (2024).
23. Kumar, P. et al. Photonically active bowtie nanoassemblies with a chirality continuum. *Nature* **615**, 418–424 (2023).
24. Petoud, S. et al. Brilliant Sm, Eu, Tb, and Dy chiral lanthanide complexes with strong circularly polarized luminescence. *J. Am. Chem. Soc.* **129**, 77–83 (2007).
25. Liu, J. et al. What makes efficient circularly polarised luminescence in the condensed phase: aggregation-induced circular dichroism and light emission. *Chem. Sci.* **3**, 2737–2747 (2012).
26. Mislow, K. & Raban, M. Stereoisomeric relationships of groups in molecules. *Topics in stereochemistry*, 1–38 (1967).
27. Mislow, K. & Siegel, J. Stereoisomerism and local chirality. *J. Am. Chem. Soc.* **106**, 3319–3328 (1984).
28. Xu, L. et al. Enantiomer-dependent immunological response to chiral nanoparticles. *Nature* **601**, 366–373 (2022).
29. Kim, J.-Y. et al. Direct-write 3D printing of plasmonic nanohelicoids by circularly polarized light. *Proc. Natl. Acad. Sci.* **121**, e2312082121 (2024).
30. Tang, Y. & Cohen, A. E. Optical chirality and its interaction with matter. *Phys. Rev. Lett.* **104**, 163901 (2010).
31. Lin, J. et al. Polarization-controlled tunable directional coupling of surface plasmon polaritons. *Science* **340**, 331–334 (2013).
32. Rodriguez-Fortuno, F. J. et al. Near-field interference for the unidirectional excitation of electromagnetic guided modes. *Science* **340**, 328–330 (2013).
33. Gong, S. H., Alpeggiani, F., Sciacca, B., Garnett, E. C. & Kuipers, L. Nanoscale chiral valley-photon interface through optical spin-orbit coupling. *Science* **359**, 443–447 (2018).
34. Sun, L. et al. Separation of valley excitons in a MoS2 monolayer using a subwavelength asymmetric groove array. *Nat. Photonics* **13**, 180–184 (2019).
35. Chen, Y. et al. Chirality-dependent unidirectional routing of WS2 valley photons in a nanocircuit. *Nat. Nanotechnol.* **17**, 1178–1182 (2022).
36. Takaishi, K., Hinoide, S., Matsumoto, T. & Ema, T. Axially chiral perixanthenoxanthenes as a circularly polarized luminophore. *J. Am. Chem. Soc.* **141**, 11852–11857 (2019).
37. Kimoto, T., Tajima, N., Fujiki, M. & Imai, Y. Control of Circularly polarized luminescence by using open-and closed-type binaphthyl derivatives with the same axial chirality. *Chem.– Asian J.* **7**, 2836–2841 (2012).
38. Takaishi, K., Iwachido, K. & Ema, T. Solvent-induced sign inversion of circularly polarized luminescence: control of excimer chirality by hydrogen bonding. *J. Am. Chem. Soc.* **142**, 1774–1779 (2020).
39. Tan, Y. B. et al. Visible circularly polarized luminescence of octanuclear circular Eu (III) helicate. *J. Am. Chem. Soc.* **142**, 17653–17661 (2020).
40. Li, Z. et al. Tailoring MoS2 valley-polarized photoluminescence with super chiral near-field. *Adv. Mater.* **30**, e1801908 (2018).
41. Duan, X. et al. Valley-addressable monolayer lasing through spin-controlled Berry phase photonic cavities. *Science* **381**, 1429–1432 (2023).
42. Liu, J. et al. Circularly polarized organic ultralong room-temperature phosphorescence with a high dissymmetry factor in chiral helical superstructures. *Adv. Mater.* **36**, 2306834 (2024).
43. Zheng, H. et al. Uncovering the circular polarization potential of chiral photonic cellulose films for photonic applications. *Adv. Mater.* **30**, 1705948 (2018).
44. Bobrovsky, A. et al. Optically and electrically controlled circularly polarized emission from cholesteric liquid crystal materials doped with semiconductor quantum dots. *Adv. Mater.* **24**, 6216 (2012).
45. Yu, H., Zhao, B., Guo, J., Pan, K. & Deng, J. Stimuli-responsive circularly polarized luminescent films with tunable emission. *J. Mater. Chem. C.* **8**, 1459–1465 (2020).

46. Shi, Y. et al. Recyclable soft photonic crystal film with overall improved circularly polarized luminescence. *Nat. Commun.* **14**, 6123 (2023).
47. Zhang, X. et al. Mechanically tunable circularly polarized luminescence of liquid crystal-templated chiral perovskite quantum dots. *Angew. Chem. Int Ed. Engl.* **136**, e202404202 (2024).
48. Choi, D. et al. Highly coherent organic lasing based on etch-free metasurface. *Nat. Commun.* **17**, 906 (2026).
49. Ge, D. et al. Hybrid plasmonic nano-emitters with controlled single quantum emitter positioning on the local excitation field. *Nat. Commun.* **11**, 3414 (2020).
50. Saito, K. & Tatsuma, T. Chiral plasmonic nanostructures fabricated by circularly polarized light. *Nano Lett.* **18**, 3209–3212 (2018).
51. Wu, Y. et al. Chiral emission from nanoscale chirotopic materials. *Figshare* https://doi.org/10.6084/m9.figshare.32347440.v1 (2026).

Acknowledgments

This work was partially carried out at the USTC Center for Micro and Nanoscale Research and Fabrication. The authors also thank Prof. Joel Yang, Prof. Zhaogang Dong and Dr. Hongtao Wang for their help in the initial sample fabrication.

Author contributions

Y.C. conceived the idea. Yawei W. and Y.C. conducted the simulations. Zhenyu W. conducted the device fabrication. Zihan W. and Y.C. performed the theoretical analysis. Yawei W. performed the optical characterization. S.H. performed the synthesis of UCNPs. J.X., M.G., Q.Z., and J.N. assisted in data processing. X.L. and Y.C. analyzed the data and wrote the manuscript with inputs from all authors. C.H., R.W., C.W., Z.L., Yiming W., D.W., and J.C. commented on and edited the manuscript. X.L. and Y.C. supervised the project.

Funding

Y.C. and Yiming W. acknowledge the support from the National Key Research and Development Project (Grant No. 2024YFA1410900). Y.C. acknowledges the support from the National Natural Science Foundation of China (Grant No. 62275241). S.H. acknowledges the support from the National Natural Science Foundation of China (Grant No. 22004087), Natural Science Foundation of Top Talent of SZTU (Grant No. 20200202) and Shenzhen Higher Education Stable Support Program (Grant No. SZWD202206). Yiming W. acknowledges the support from the National Natural Science Foundation of China (Grant Nos. 52372156, 62288102). D.W. acknowledges the support from the National Key Research and Development Project (Grant No. 2021YFF0502700) and the National Natural Science Foundation of China (Grant No. 62325507, 61927814).

Competing interests

The authors declare no competing interests.

Additional information

Supplementary information The online version contains supplementary material available at https://doi.org/10.1038/s41467-026-74088-8.

Correspondence and requests for materials should be addressed to Xiaogang Liu or Yang Chen.

Peer review information *Nature Communications* thanks the anonymous reviewers for their contribution to the peer review of this work. A peer review file is available.